

Article

Continuous-Flow Hydrogenation of Nitroaromatics in Microreactor with Mesoporous Pd@SBA-15

Kejie Chai ^{1,2}, Runqiu Shen ^{1,2}, Tingting Qi ^{1,2}, Jianli Chen ^{1,3} , Weike Su ^{1,2,*} and An Su ^{4,*} 

¹ National Engineering Research Center for Process Development of Active Pharmaceutical Ingredients, Collaborative Innovation Center of Yangtze River Delta Region Green Pharmaceuticals, Zhejiang University of Technology, Hangzhou 310014, China

² Key Laboratory of Pharmaceutical Engineering of Zhejiang Province, Zhejiang University of Technology, Hangzhou 310014, China

³ College of New Materials Engineering, Jiaying Nanhu University, Jiaying 314000, China

⁴ College of Chemical Engineering, Zhejiang University of Technology, Hangzhou 310014, China

* Correspondence: suweike@zjut.edu.cn (W.S.); ansu@zjut.edu.cn (A.S.)

Abstract: The hydrogenation of nitroaromatics to prepare aromatic amines plays a crucial role in the chemical industry. Traditional hydrogenation has the risk of hydrogen leakage from the equipment, and its catalyst has the disadvantage of being easily deactivated and difficult to recover. In this study, we designed an efficient and stable mesoporous catalyst, Pd@SBA-15, which was constructed by impregnating the nanopores of the mesoporous material SBA-15 with palladium nanoparticles. The catalyst was then filled in a micro-packed-bed reactor (MPBR) for continuous flow hydrogenation. The designed continuous flow hydrogenation system has two distinctive features. First, we used mesoporous Pd@SBA-15 instead of the traditional bulk Pd/C as the hydrogenation catalyst, which is more suitable for exposing the active sites of metal Pd and reducing the agglomeration of nanometals. The highly ordered porous structure enhances hydrogen adsorption and thus hydrogenation efficiency. Secondly, the continuous flow system allows for precise detection and control of the reaction process. The highly efficient catalysts do not require complex post-treatment recovery, which continues to operate for 24 h with barely any reduction in activity. Due to the high catalytic activity, the designed mesoporous Pd@SBA-15 showed excellent catalytic performance as a hydrogenation catalyst in a continuous flow system with 99% conversion of nitroaromatics in 1 min. This work provides insights into the rational design of hydrogenation systems in the chemical industry.

Keywords: Pd@SBA-15; mesoporous material; continuous flow; hydrogenation; nitroaromatics



Citation: Chai, K.; Shen, R.; Qi, T.; Chen, J.; Su, W.; Su, A.

Continuous-Flow Hydrogenation of Nitroaromatics in Microreactor with Mesoporous Pd@SBA-15. *Processes* **2023**, *11*, 1074. <https://doi.org/10.3390/pr11041074>

Academic Editor: Adam Smoliński

Received: 20 February 2023

Revised: 22 March 2023

Accepted: 29 March 2023

Published: 3 April 2023



Copyright: © 2023 by the authors. Licensee MDPI, Basel, Switzerland. This article is an open access article distributed under the terms and conditions of the Creative Commons Attribution (CC BY) license (<https://creativecommons.org/licenses/by/4.0/>).

1. Introduction

The hydrogenation of nitroaromatics to prepare aromatic amines is a crucial reaction in industry widely used in the synthesis of pharmaceuticals, dyes, and cosmetics [1–5]. From an environmental and economic point of view, hydrogen is an optimal choice for hydrogenation reagents [6]. However, traditional intermittent hydrogenation systems present high safety risks, energy consumption, and pollution, such as hydrogen leakage due to heavy operation and high pressure, which are considered incompatible with the concept of green chemistry [7]. Compared with intermittent reactors, continuous flow reactors have unique advantages, including better heat and mass transfer, smaller reaction volume, and smoother reaction conditions, which significantly improve the intrinsic safety of the reactions [8]. Over the past decade, the use of continuous flow reactors in hydrogenation, nitration, and diazotization reactions has become increasingly common [9–11]. Lebl et al. developed a novel type of catalytic static mixer with a rectangular cross-section coated with Pd/Al₂O₃ [12]. The catalytic static mixers showed excellent catalytic performance in the continuous flow hydrogenation of nitroaromatics and were applied to the synthesis of a key intermediate for the medicine tizanidine. Braun et al. reported a tungsten monocarbide

(WC) obtained through a urea glass route with high activity and chemoselectivity for the continuous flow hydrogenation of nitro compounds [13]. Moreover, they extended WC and prepared a bimetallic Ni@WC composite characterized by high activity for the cardanol hydrogenation. Although continuous flow reactors have shown many excellent applications in the field of hydrogenation, they still have technical challenges to overcome when it comes to heterogeneous catalyzes, such as improving catalytic efficiency and maintaining catalyst stability.

The catalyst is a core factor in optimizing the hydrogenation of nitroaromatics, whether it is an intermittent reactor for traditional hydrogenation or a microreactor for continuous-flow hydrogenation [14–16]. Couto et al. reviewed the performance of a series of commercially available hydrogenation catalysts for nitrobenzene [17]. Although some of these catalysts showed relatively good short-term hydrogenation activity, there remained a proportion of catalysts prone to deactivation, as traditional metal catalysts tended to aggregate during application. In the case of microreactors, the packed bed is typically operated for a long time, which makes the catalyst activity and lifetime critical [18–20]. Therefore, there is an urgent need to prepare a highly efficient and stable catalyst for continuous-flow hydrogenation systems. Mesoporous materials are an ideal class of supported materials due to their collapse resistance, large specific surface area, and tunable pore size [21,22]. The large specific surface area facilitates gas adsorption, metal dispersion, and active site exposure, thereby enhancing catalytic activity [23–27]. Liu et al. designed and synthesized a group of ternary Ni–Cr–Al metal oxide composites with an ordered mesoporous structure and tested them for CO methanation to produce synthetic natural gas (SNG) [28]. The optimized ordered mesoporous Ni–Cr–Al catalysts showed better properties of anti-coking and anti-sintering, as well as higher catalytic activity and stability than the traditional Ni catalysts. Xun et al. prepared a group of catalysts of WO_3 highly dispersed on mesoporous ZrO_2 by hydrothermal treatment and calcination [29]. The obtained $700\text{-C}_{16}\text{-WO}_3/\text{ZrO}_2$ showed excellent catalytic activity in oxidation desulfurization, and the dibenzothiophene in the model oil could be completely oxidized to dibenzothiophene sulfone. Mesoporous materials are thus an important class of catalysts in the field of catalysis and still hold great potential to exploit.

In this work, we reported the synthesis of a new hydrogenation catalyst Pd@SBA-15 by an impregnation method that loaded the metal Palladium (Pd) onto the mesoporous material SBA-15 (Figure 1). The active sites and surface area of the mesoporous structure were characterized. The catalyst was then filled into a micro-packed-bed reactor (MPBR) for the continuous-flow hydrogenation of nitroaromatics. The conversion and selectivity of the reactions were optimized, and the stability of the catalyst was also tested. In addition, we also evaluated the scope of this catalysis by varying the functional groups on the nitrobenzene ring.

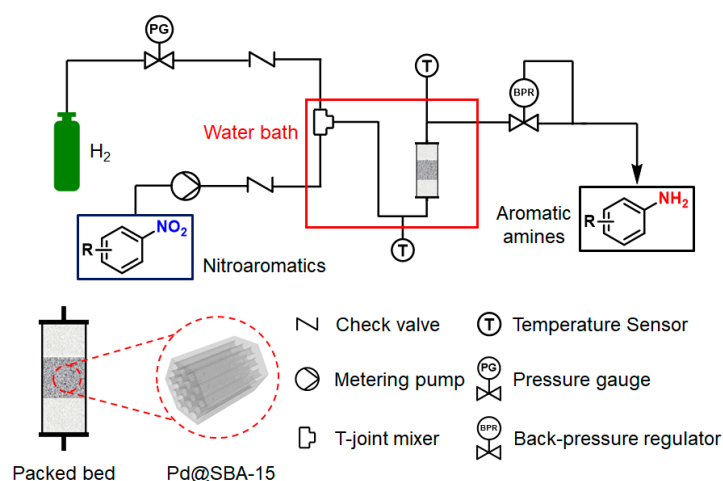


Figure 1. The microreactor of continuous-flow hydrogenation with mesoporous Pd@SBA-15.

2. Materials and Methods

Materials. All chemical reagents with the analytical grade were purchased from Sinopharm Chemical Reagent Co. (Shanghai, China) without further purification. Poly(ethylene glycol)-block-poly(propylene glycol)-block-poly(ethylene glycol) (average Mn~5800) (Pluronic®P-123), tetraethyl orthosilicate (TEOS) (28.4% SiO₂), hydrochloric acid (HCl) (12 M), cyclohexane (99.7%), ethanol (EtOH, anhydrous, 99.7%), palladium(II) chloride (99%, 5% Pd), methanol (MeOH, AR), ethyl acetate (EA, AR), tetrahydrofuran (THF, AR), acetonitrile (MeCN, AR), dimethylformamide (DMF, AR), silicon dioxide (100–200 mesh), palladium/carbon (Pd/C, 5% (w/w) on carbon), nitrobenzene (99%), 4-nitrotoluene (99%), 3-nitrotoluene (98%), 2-nitrotoluene (99%), 4-nitrophenol (99%), 3-nitrophenol (99%), 2-nitrophenol (99%), 4-nitroanisole (98%), 2-nitroanisole (99%), 4-nitrobenzoic acid (99%), 3-nitrobenzoic acid (99%), 2-nitrobenzonitrile (98%), 2-nitrobenzaldehyde (99%), 4'-nitroacetophenone (98%), 4-nitrobenzamide (98%), 2-methoxy-5-nitropyridine (98%), and 5-nitropyridine-2-carboxylic acid (97%). H₂ (99.999%) was purchased from Hangzhou Jingong Special Gas Co., Ltd. (Hangzhou, China).

Synthesis of Pd@SBA-15. Mesoporous silica template SBA-15 was synthesized following the conventional method reported in the literature [30]. A total of 0.1 g of PdCl₂ was added to 10 g of 12 M HCl to dissolve completely. Next, 1 g of SBA-15 was added to the solution and stirred continuously at a constant temperature of 80 °C until the solution was completely evaporated. The solid obtained after evaporation was loaded into a quartz boat in a quartz tube. The quartz tube was placed in a preheated tube furnace at 350 °C for 4 h with a continuous hydrogen gas flow (flow rate = 150 mL min⁻¹). Then, the tube furnace was cooled to room temperature, and the catalyst Pd@SBA-15 was obtained. The Pd@SBA-15 obtained was immediately stored in a vacuum-drying oven to prevent the influences of water and oxygen in the environment.

Hydrogenation in a micro pack-bed reactor (MPBR). The synthetic Pd@SBA-15 was loaded into an HPLC column (5 mm diameter and 50 mm long), and the ends were filled with silicon dioxide. Then, the HPLC column was sealed with sealing nuts, and the MPBR was obtained. The entire MPBR was placed vertically in a water bath for precise temperature control. The feedstock was dissolved in the solvent and pumped into the microreactor via a metering pump. The hydrogen was controlled by a hydrogen pressure gauge. Two check valves prevent backflow of gas and liquid. The hydrogen and the solution were mixed in a T-joint mixer before entering the inlet of the MPBR. The gas–liquid mixture was then hydrogenated in the MPBR, and the hydrogenation temperature was controlled by a water bath. All tubing was stainless steel with an outside diameter of 1/16". A manual back-pressure regulator was placed at the outlet of the reactor to control system pressure. Due to the presence of check valve and back-pressure regulator, the continuous-flow system is almost completely isolated from air. The reaction conditions were optimized by adjusting parameters such as hydrogen pressure, flow rate, and temperature.

Purification and yield determination. The experimental yield of the product was determined by high-performance liquid chromatography (HPLC) using external standard method. HPLC detection conditions: HPLC Column (XB-C18, 10 μm, Dim 4.6 × 250 mm), mobile phase (isocratic elution, H₂O:MeOH = 40:60), flow rate (1.00 mL/min), ultraviolet wavelength (254 nm), and chromatographic column temperature (30 °C). After purification by silica gel column chromatography and removal of the solvent, the mass of the isolated product was obtained. Then, the isolated yield and the production rate were calculated by Equations (1) and (2), respectively:

$$\text{isolated yield} = \frac{m_{\text{isolated}}}{C_0 F_0 t M_{\text{isolated}}} \quad (1)$$

$$\text{production rate} = \frac{m_{\text{isolated}}}{t} \quad (2)$$

where m_{isolated} is the mass of the isolated product by silica gel column chromatography during run time; C_0 is the concentration of the feedstock in the solution; F_0 is the flow rate

of the solution; t is the continuous-flow system run time; $M_{isolated}$ is the relative molecular mass of the isolated product. Finally, the molecular structures of all products were further determined by nuclear magnetic resonance (NMR).

Characterization. X-ray diffraction (XRD) characterization was performed using a Bruker D8 Advance X-ray diffractometer (Bruker, Billerica, MA, USA) with Cu K α irradiation ($\lambda = 1.5406 \text{ \AA}$). Scanning electron microscopy (SEM) and energy-dispersive X-ray spectrometer (EDS) characterization were measured by using a FEI Nano SEM430 measurement (FEI, New York, NY, USA). Transmission electron microscopy (TEM) measurements were performed using an HT-7700 apparatus (Hitachi, Chiyoda, Japan). The high-resolution TEM (HRTEM) images with the selected area electron diffraction (SAED) patterns were collected using a JEM 2100 instrument (Japan Electron Optics Laboratory, JEOL, Akishima, Japan). N₂ physisorption isotherms were recorded using a TriStar II 3020 instrument (Micromeritics Instrument Corporation, Norcross, GA, USA) at $-196 \text{ }^\circ\text{C}$. X-ray photoelectron spectroscopy (XPS) spectrums were collected using a Thermo Scientific Escalab 250Xi apparatus (Thermo Fisher Scientific, Waltham, MA, USA) with a monochromatic Al K α X-ray source. Inductively coupled plasma optical emission spectrometer (ICP-OES) analysis was performed using an Agilent 5110 instrument (Agilent, Santa Clara, CA, USA). Inductively coupled plasma mass spectrometry (ICP-MS) analysis was performed using a PerkinElmer NexION 1000 instrument (PerkinElmer, Waltham, MA, USA). High-performance liquid chromatography (HPLC) characterization was measured by using an Agilent 1100 Series instrument (Agilent, Santa Clara, CA, USA). Nuclear magnetic resonance (NMR) analysis was performed using a Bruker Avance III 500 MHz instrument (Bruker, Billerica, MA, USA) and a Bruker Avance III HD 600 MHz instrument (Bruker, Billerica, MA, USA).

3. Results and Discussion

Characterization of Pd@SBA-15. In this work, the mesoporous silica SBA-15 was prepared in the first step by following the conventional hydrothermal method and used in the second step as the supported material for the synthesis of the highly efficient catalyst Pd@SBA-15 by impregnation method. The XRD patterns of SBA-15 and Pd@SBA-15 fabricated in this work are collected and listed in Figure 2. The small angle XRD patterns (Figure 2a) of SBA-15 and Pd@SBA-15 both show clear diffraction peaks at 0.89° , 1.53° , 1.76° , 2.33° , and 2.67° in the region of $2\theta = 0.5\text{--}5.0^\circ$, which can be indexed to (100), (110), (200), (300), and (220) planes of mesoporous silica materials with highly ordered 2-dimensional $p6mm$ hexagonal symmetry [31,32]. Pd@SBA-15 shows an almost identical pattern to SBA-15, which demonstrates that both the mesostructure and nanostructure of the mesoporous material SBA-15 are both well preserved during the loading process. The wide-angle XRD patterns (Figure 2b) of SBA-15 and Pd@SBA-15 both show a weak and broad diffraction peak at 2θ value of approximately 23° , as the silica prepared by the sol-gel process is always in an amorphous state [31]. In addition, the wide-angle XRD pattern (Figure 2b) of the Pd@SBA-15 also shows clear diffraction peaks at 40.0° , 46.5° , 68.1° , and 82.0° , which can be indexed to the (111), (200), (220), and (311) planes of Pd⁰ (JCPDS Card 00-087-0643). This demonstrates that Pd⁰ is loaded on SBA-15 with a good degree of crystallinity.

The N₂ adsorption-desorption isotherms for SBA-15 and Pd@SBA-15 (Figure 2c,d) show type IV isotherms with an H1 hysteresis loop related to the capillary condensation step, characteristic of mesoporous materials with highly uniform pore size distributions [33]. This is further evidence that the mesostructure is still preserved, which is consistent with the XRD characterization. The specific surface area of SBA-15 and Pd@SBA-15 was calculated as $550 \pm 7.13 \text{ m}^2 \text{ g}^{-1}$ and $357 \pm 2.77 \text{ m}^2 \text{ g}^{-1}$, respectively, using the Brunauer-Emmett-Teller (BET) method. Meanwhile, the mean pore size (Figure 2e,f) of SBA-15 and Pd@SBA-15 was $5.67 \pm 0.41 \text{ nm}$ and $4.35 \pm 0.54 \text{ nm}$, respectively, calculated by the Barret-Joyner-Halenda (BJH) method. In addition, the specific surface area and the mean pore size measurements were performed on SBA-15 after it had been treated similarly to the Pd@SBA-15 catalyst, i.e., the entire Pd@SBA-15 synthesis process without the addition of PdCl₂, which was $512 \pm 5.03 \text{ m}^2 \text{ g}^{-1}$ and $5.59 \pm 0.30 \text{ nm}$ (Figure S1a,b). It indicates that the acid, heat, stirring,

and reduction treatments only slightly reduce the specific surface area and the mean pore size of SBA-15 without Pd nanoparticles. Therefore, the reason for the significant reduction in specific surface area and mean pore size after loading the mesoporous material SBA-15 with Pd nanoparticles could be that part of the pore channel was occupied by the metal Pd nanoparticles. This indicates that the metal Pd occupies part of the pore channel, which leads to a reduction in specific surface area and mean pore size.

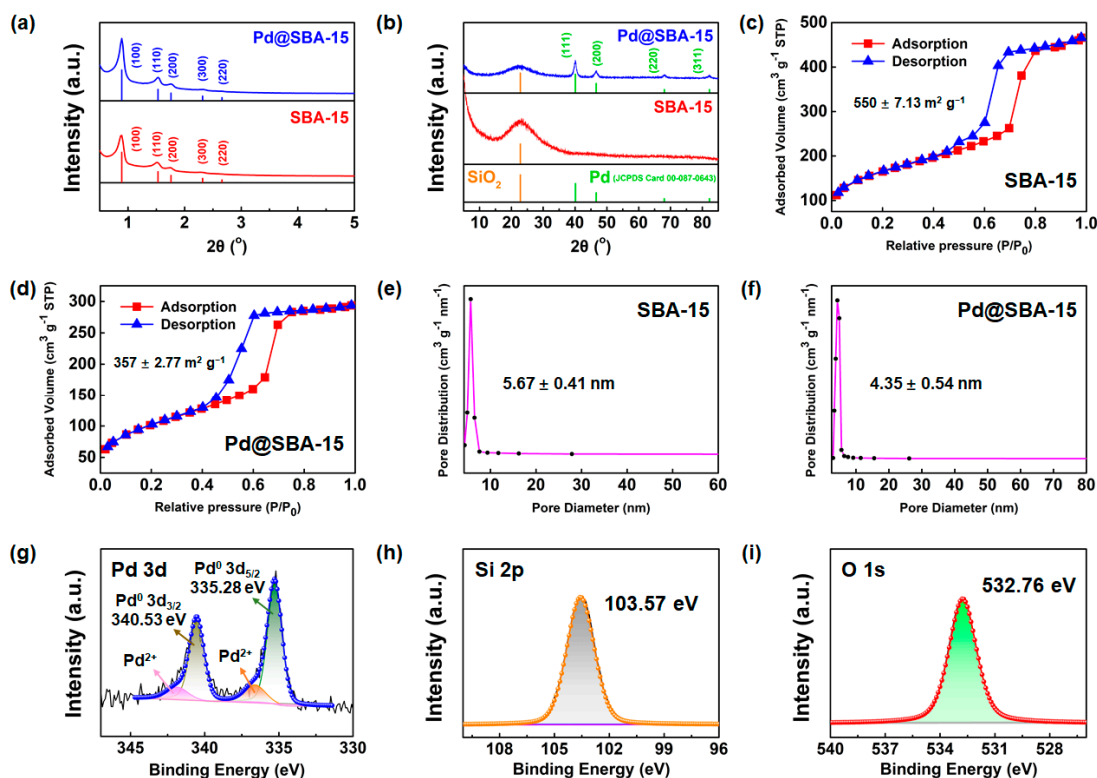


Figure 2. (a) Small-angle XRD pattern of Pd@SBA-15 and SBA-15; (b) Wide-angle XRD pattern of Pd@SBA-15 and SBA-15; N₂ adsorption–desorption isotherms for (c) SBA-15 and (d) Pd@SBA-15; Pore size distributions of (e) SBA-15 and (f) Pd@SBA-15; XPS spectrums of Pd@SBA-15: (g) Pd 3d, (h) Si 2p, and (i) O 1s.

The composition and chemical states of the products are investigated by XPS analysis (Figure 2). Spectrums were analyzed using XPSPEAK (Version 4.1), and the background response of the peaks was removed with the Shirley algorithm. The position of the lowest binding energy peak of the C 1s (the adventitious carbon) was measured, and its difference with the theoretical value (284.8 eV) was calculated. All XPS spectrums were corrected by subtracting this difference. The Pd 3d spectrum (Figure 2g) contains 2 main peaks at 340.53 eV and 335.28 eV with a 5.25 eV spacing, which matches the Pd 3d_{3/2} and Pd 3d_{5/2} of Pd⁰ [34,35]. In addition, the Pd 3d spectrum exhibits two weak peaks of Pd²⁺, which possibly results from the surface oxidation of Pd metal [35]. The Si 2p and O 1s spectrums (Figure 2h,i) show peaks at 103.57 eV and 532.76 eV, representing the Si⁴⁺ state and O²⁻ state [36] and demonstrating the presence of SiO₂. The absence of the Pd 3p_{3/2} peak overlapping with the O 1s peak could be the low loading of Pd on SBA-15 [35].

SEM and TEM images (Figure 3a–c) reveal that the overall external structure of the synthesized Pd@SBA-15 resembles a stack of rice grains. However, its interior has a regular arrangement of pores and an even more regular honeycomb shape in the cross-section, demonstrating the conservation of the mesoporous structure [33]. Compared to traditional bulk Pd/C catalysts (Figure 3d), the pore structure provides more active sites, enhances hydrogen adsorption, and largely avoids the aggregation of nanometals. In the HRTEM image (Figure 3e), the well-resolved lattice fringes confirm that the Pd is well crystallized. The

image also shows an interlayered spacing of 0.2256 nm, which corresponds to the d spacing of (111) crystal planes of Pd, and the metal Pd is loaded as nanoparticles. The SAED pattern (Figure 3f) shows clear diffraction rings indexed to the (111), (200), (220), and (311) planes of Pd⁰, which is consistent with the XRD results in Figure 2b. The ring-shaped spots array of various planes demonstrates their polycrystalline structure, and the dominant exposed plane of (111) indicates the presence of anisotropy in shape, which facilitates increasing the catalytic activity of Pd [37–40]. The spots are slightly dispersed because the metal Pd disperses into mesoporous pores, which brings many crystal defects and produces more active sites. The EDS elemental mappings (Figure 3g) indicate that the distributions of Si and O are homogeneous, and the Pd is uniformly spotted on the surface of the carrier. The content of Pd loading on SBA-15 investigated by ICP-OES (Table S1) was around 5% (w/w).

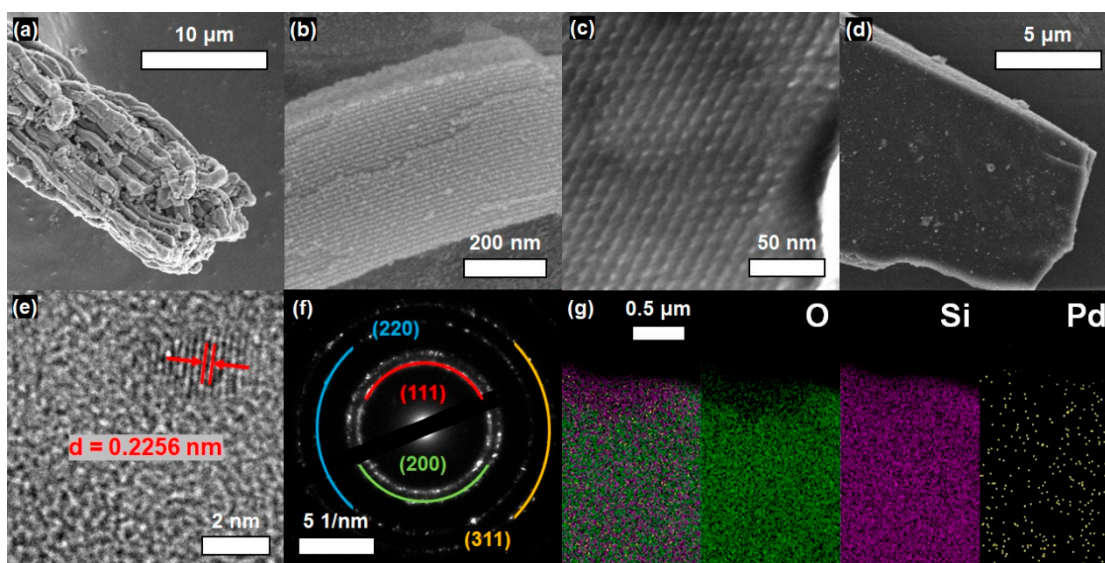


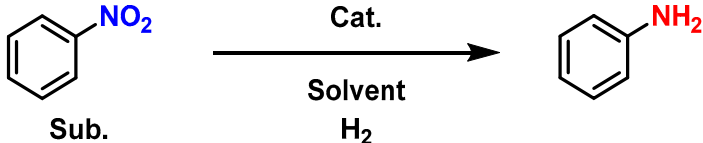
Figure 3. Pd@SBA-15: (a,b) SEM images and (c) TEM image; Pd/C: (d) SEM image; Pd@SBA-15: (e) HRTEM image, (f) SAED pattern, and (g) EDS elemental mappings.

Continuous-flow hydrogenation. In this work, a more environmentally friendly and practical continuous-flow hydrogenation system was developed by using a micro-packed-bed reactor (MPBR) filled with Pd@SBA-15 as a reusable catalytic model. Aromatic amines were prepared by a safe and efficient hydrogenation process using nitroaromatics and hydrogen as feedstock. In the optimization of reaction parameters, the reaction was carried out with methanol as the solvent. The yield of the aniline reached 85%, 96%, 99%, and 99% under the reaction temperature being 40 °C, 50 °C, 60 °C, and 70 °C, respectively (Table 1, entries 1–4). By further adjusting the flow rate from 0.25 to 1.00 mL/min, the nitrobenzene could be completely hydrogenated at a flow rate of 0.5 mL/min (Table 1, entries 3, 5–7), representing that the optimal residence time of this continuous-flow system was 1.0 min. By slightly increasing the H₂ pressure to 3.0 MPa, the yield barely increased, representing that the H₂ pressure was sufficient (Table 1, entries 8–9).

The yield of aniline decreased to 23%, 31%, and 52% when ethanol, ethyl acetate, and acetonitrile were used as the solvent, respectively (Table 1, entries 10–12). When tetrahydrofuran replaced methanol as the solvent, the yield was significantly reduced and close to zero (Table 1, entry 13), as was the result obtained with dimethylformamide (Table 1, entry 14). Hydrogen had a higher solubility in methanol, and hydrogenation had a higher activity coefficient when methanol was used as a solvent, which had been studied and reported in the literature [41]. Thus, the results of the optimized solvent indicated that methanol was the optimized solvent in this hydrogenation. The palladium loading of the Pd@SBA-15 was around 5% (w/w), investigated by ICP-OES, as shown in Table S1. This was a very important characterization parameter for evaluating catalytic

performance. The Pd/C (5% (*w/w*) on carbon) was purchased from Sinopharm Chemical Reagent Co. without further purification. Therefore, the Pd@SBA-15 and Pd/C had the same Pd loading. Although the Pd nanoparticle's size/shape could not be precisely controlled, it was also attributed to the structure of the mesoporous material SBA-15 because of the conventional impregnation method used. Meanwhile, hydrogen adsorption and exposure of the active site both depended on the structure of the Pd@SBA-15 and the Pd/C. For the substrate, nitrobenzene was chosen without any additional electron-withdrawing or electron-donating groups. Therefore, when the catalyst was replaced by traditional bulk Pd/C, the yield was only 83% (Table 1, entry 15), indicating that mesoporous structure could improve the catalytic activity of Pd@SBA-15.

Table 1. Optimization of the conditions for the synthesis of aniline.



Entry ^a	Flow Rate (mL/min)	H ₂ Pres. (MPa)	Temp. (°C)	Solvent	Yield (%) ^b
1	0.50	1.0	40	MeOH	85
2	0.50	1.0	50	MeOH	96
3	0.50	1.0	60	MeOH	99
4	0.50	1.0	70	MeOH	99
5	0.25	1.0	60	MeOH	99
6	0.75	1.0	60	MeOH	95
7	1.00	1.0	60	MeOH	88
8	0.50	2.0	40	MeOH	85
9	0.50	3.0	40	MeOH	85
10	0.50	1.0	60	EtOH	23
11	0.50	1.0	60	EA	31
12	0.50	1.0	60	MeCN	52
13	0.50	1.0	60	THF	trace
14	0.50	1.0	60	DMF	trace
15 ^c	0.50	1.0	60	MeOH	83

^a Reaction conditions: substrate (0.1 mol/L), catalyst (Pd@SBA-15, 0.1 g), and back-pressure (0.9 MPa). ^b The experimental yields were determined by HPLC. ^c The catalyst was traditional bulk Pd/C (0.1 g).

According to the above results, the optimized flow rate, H₂ pressure, reaction temperature, residence time, and solvent were set to 0.50 mL/min, 1.0 MPa, 60 °C, 1.0 min, and methanol.

The scope of this hydrogenation was then investigated by using various nitroaromatics with different functional groups as the reactants (Table 2). First, the compatibility of different functional groups on the nitrobenzene ring was studied. Under optimal reaction conditions, regardless of the ortho, meta, or para substituent groups, the electron-withdrawing and electron-donating groups were well compatible in this reaction, which matched the expectations from the literature [6,15,16,42–50]. Therefore, the corresponding target products were able to achieve high yields (Table 2, entries 1–15). Notably, when more than one unsaturated group was present, only the nitro was hydrogenated tested by HPLC, indicating that the catalyst was highly selective for the nitro group (Table 2, entries 10–15). In addition, when nitropyridines were used as the reactants, the corresponding products could also be successfully synthesized in high yields by this hydrogenation process (Table 2, entries 16–17), indicating it was a universal continuous-flow hydrogenation method. Similar to the aniline synthesis, the electron-withdrawing and electron-donating groups did not affect the hydrogenation of nitropyridines. Furthermore, the highly concentrated synthesis of aniline was carried out and resulted in a good yield, demonstrating

the value of this hydrogenation system (Table 2, entry 18). After purification by silica gel column chromatography and removal of the solvent, the mass of the isolated product was obtained. Then, the isolated yields and the production rates of the obtained products were calculated and listed in Scheme S1. The molecular structures of all products were further characterized by NMR in the Supporting Information. The above results showed that this continuous-flow catalytic hydrogenation system had good functional group tolerance and was demonstrated to be a practical method for the synthesis of amine products in high yields.

Table 2. Continuous-flow hydrogenation of various nitroaromatics using Pd@SBA-15.

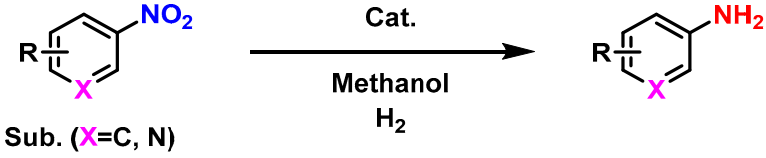
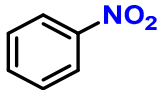
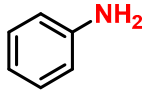
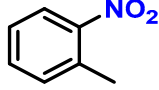
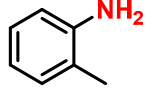
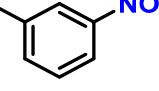
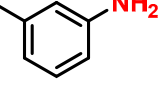
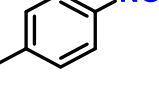
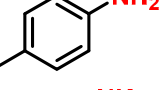
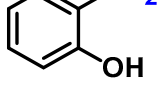
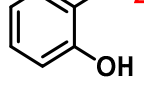
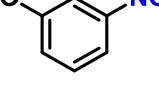
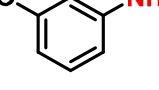
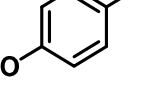
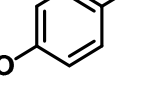
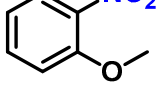
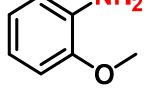
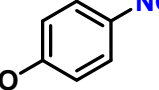
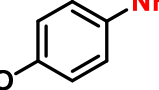
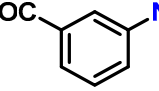
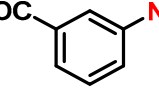
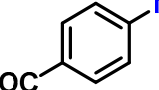
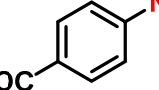
				
Entry ^a	Substrate	Product		Yield (%) ^b
1			(2a)	99
2			(2b)	99
3			(2c)	99
4			(2d)	99
5			(2e)	99
6			(2f)	99
7			(2g)	99
8			(2h)	99
9			(2i)	99
10			(2j)	99
11			(2k)	99

Table 2. Cont.

Sub. (X=C, N)			
Entry ^a	Substrate	Product	Yield (%) ^b
12			98
13			98
14			99
15			98
16			99
17			99
18 ^c			98

^a Reaction conditions: substrate (0.1 mol/L, methanol as solvent), catalyst (Pd@SBA-15, 0.1 g), flow rate (0.50 mL/min), H₂ (1.0 MPa), back-pressure (0.9 MPa), 60 °C, and 1.0 min. ^b The experimental yields were determined by HPLC. ^c The highly concentrated reaction conditions: nitrobenzene (2.0 mol/L, methanol as solvent), catalyst (Pd@SBA-15, 2.0 g), flow rate (0.50 mL/min), H₂ (1.0 MPa), back-pressure (0.9 MPa), 60 °C, and 1.0 min.

After demonstrating the substrate compatibility, the stability of this catalyst in the continuous-flow system was further examined. Continuous operation of the hydrogenation with Pd@SBA-15 as the catalyst for 24 h at 50 °C, which ensures no overdose of the catalyst. The results show that the yield of aniline remains at around 96% (Figure 4) with no obvious decrease, indicating that Pd@SBA-15 can remain stable for at least 24 h. The ICP-MS analysis shows that the metal Pd is almost absent from the reaction solution after 24 h, indicating that barely any leaching of Pd from the catalyst occurs (Table S1).

In addition, the Pd@SBA-15 was analyzed again after 24 h of reaction. The TEM image (Figure S2) shows that the interior of Pd@SBA-15 remains a regular porous structure, and there are no obvious metal particles, which means that the mesoporous structure remains after 24 h of reaction and there is barely any aggregation of metal Pd. The small angle XRD pattern (Figure S3) of Pd@SBA-15 still shows (100), (110), (200), (300), and (220) planes of mesoporous structure at $2\theta = 0.99^\circ, 1.61^\circ, 1.85^\circ, 2.42^\circ,$ and 2.74° , which is consistent with the TEM characterization. Meanwhile, the wide-angle XRD pattern (Figure S4) shows diffraction peaks at 2θ value of approximately 23° , which is indexed to amorphous state

SiO_2 , and $2\theta = 39.9^\circ$, 46.4° , 67.8° , and 81.8° , which are indexed to the (111), (200), (220), and (311) planes of Pd^0 (JCPDS Card 00-087-0643) [31]. Moreover, the valence states of the Pd@SBA-15 are investigated by XPS analysis (Figure S5). The Pd 3d, Si 2p, and O 1s spectrums measured over the catalyst after 24 h of reaction are almost identical to the ones measured before the reaction (Figure 2). The XRD and XPS analysis means that the catalyst is still composed of Pd^0 and SiO_2 . The EDS elemental mappings (Figure S6) indicate that the Pd remains uniformly distributed on the SBA-15 carrier, and the ICP-OES analysis (Table S1) shows that the content of Pd loading on SBA-15 was still around 5% (*w/w*) after 24 h of reaction. They further demonstrate the stability of the Pd@SBA-15 . In addition, the catalyst does not need to be separated and recovered, which was a great advantage of the combination of the heterogeneous catalyst and the microreactor.

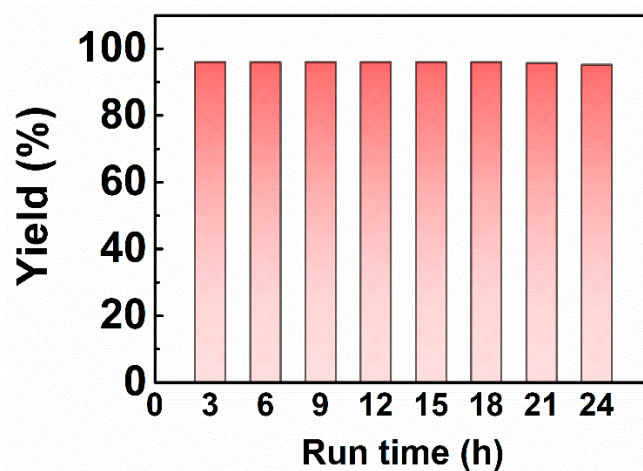


Figure 4. Run time of continuous-flow hydrogenation in microreactor. Reaction conditions: nitrobenzene (0.1 mol/L, methanol as solvent), catalyst (Pd@SBA-15 , 0.1 g), flow rate (0.50 mL/min), H_2 (1.0 MPa), back-pressure (0.9 MPa), 50°C , and 1.0 min.

The mechanism of hydrogenation of nitroaromatics using metal Pd-based catalysts has been extensively studied in the literature [51–53]. It is generally accepted that hydrogenation follows a multi-step mechanism (Figure 5). First, the nitroaromatics (I) combine with the dissociated H on the catalyst surface. The hydrogenation then proceeds in multiple steps to form aromatic amines (VII), which involves multiple intermediates, such as nitroso (II), hydroxylamine (III), azoxy (IV), azo (V), and hydrazo (VI) derivatives. The reduction of nitroso (II) to hydroxylamine (III) occurs rapidly and is, therefore, the direct route of hydrogenation [53]. In addition, nitroso (II) and hydroxylamine (III) undergo combining in hydrogenation accompanied by electron transfer [54]. The indirect route leads progressively to the formation of three intermediates, azoxy (IV), azo (V), and hydrazo (VI) [53]. Ultimately, the hydrogenation product of both pathways is aromatic amines (VII). Both N_2 physisorption and electron microscopy have demonstrated that Pd@SBA-15 has a highly regular porous structure, which facilitates hydrogen adsorption. In addition, the catalytic activity of Pd@SBA-15 was found to be higher than that of traditional bulk Pd/C. Therefore, these unstable intermediates react rapidly during the hydrogenation until the formation of aromatic amines.

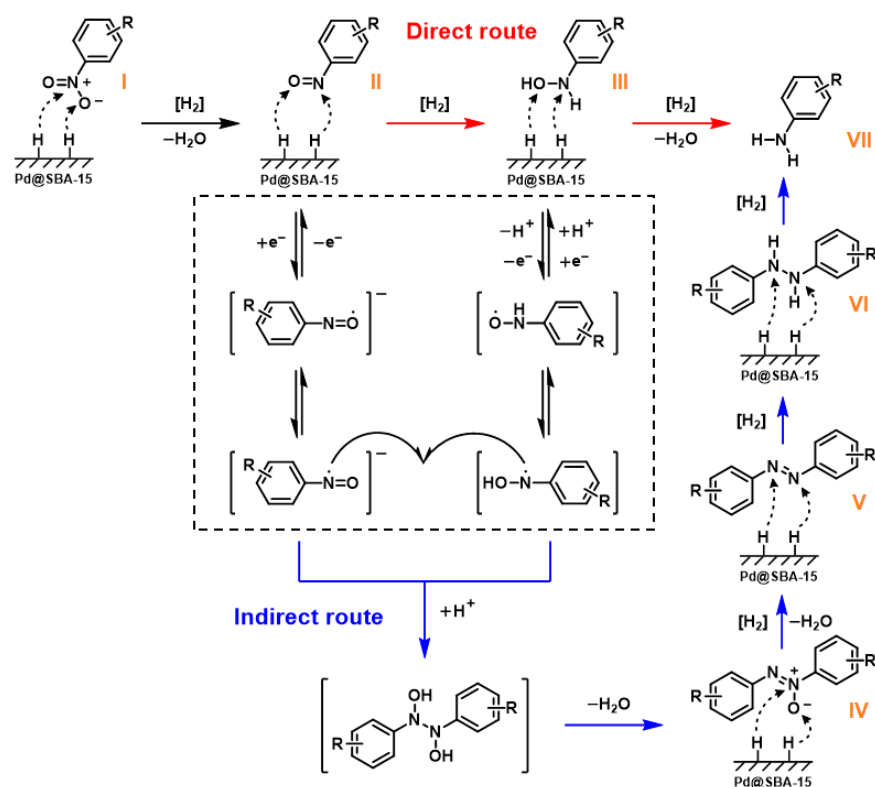


Figure 5. General mechanism for the nitroaromatics hydrogenation.

4. Conclusions

The design and synthesis of a mesoporous Pd@SBA-15 with highly ordered nanopores via an impregnation method were reported, as well as its application to heterogeneous catalysis of the hydrogenation of nitroaromatics in a continuous-flow system. The efficient and stable catalytic performances of the mesoporous Pd@SBA-15 should be attributed to the Pd nanoparticles not aggregating easily, and hydrogen can easily adsorb to participate in the reaction, which is enabled by structurally stable mesoporous material SBA-15 accompanied by highly ordered nanopore channels. The obtained Pd@SBA-15 showed excellent catalytic performance for the hydrogenation of nitroaromatics to prepare aromatic amines, with a conversion of 99% achieved, beyond the traditional bulk Pd/C. This work has important implications for the combination of mesoporous materials and continuous-flow reactions. Although the semi-industrial scale reaction has not been attempted in this study, one of the advantages of the continuous-flow microreactors is the easiness of scale-up due to their smaller scale-up effects compared to intermittent reactors. A simple way of scaling up is to parallelly arrange a number of channels or reactors [55–57].

Supplementary Materials: The following supporting information can be downloaded at: <https://www.mdpi.com/article/10.3390/pr11041074/s1>, Table S1: The content of Pd investigated by ICP-OES/MS; Figure S1: (a) N₂ adsorption-desorption isotherms and (b) pore size distribution of the SBA-15 treated similarly to the entire Pd@SBA-15 synthesis process without the addition of PdCl₂; Figure S2: TEM image of Pd@SBA-15 after 24 h of reaction; Figure S3: Small angle XRD pattern of Pd@SBA-15 after 24 h of reaction; Figure S4: Wide-angle XRD pattern of Pd@SBA-15 after 24 h of reaction; Figure S5: XPS spectrums of Pd@SBA-15 after 24 h of reaction: (a) Pd 3d, (b) Si 2p, (c) O 1s; Figure S6: EDS elemental mappings of Pd@SBA-15 after 24 h of reaction; Scheme S1: Isolated yields and production rates of the obtained products; Synthesis of SBA-15; Characterization of the products; Copies of ¹H and ¹³C NMR Spectra.

Author Contributions: Conceptualization, K.C., W.S. and A.S.; Data curation, K.C. and T.Q.; Formal analysis, T.Q.; Funding acquisition, W.S. and A.S.; Investigation, K.C., R.S., T.Q. and J.C.; Methodology, K.C., R.S., J.C., W.S. and A.S.; Project administration, W.S. and A.S.; Resources, J.C.; Supervision, W.S.; Validation, K.C., R.S., T.Q. and J.C.; Visualization, R.S., T.Q. and A.S.; Writing—original draft, K.C.; Writing—review and editing, R.S., J.C., W.S. and A.S. All authors have read and agreed to the published version of the manuscript.

Funding: We gratefully acknowledge Zhejiang Province Science and Technology Plan Project (No. 2019-ZJ-JS-03 and No. 2022C01179) for financial support.

Institutional Review Board Statement: Not applicable.

Informed Consent Statement: Not applicable.

Data Availability Statement: The data presented in this study are available in [Continuous-Flow Hydrogenation of Nitroaromatics in Microreactor with Mesoporous Pd@SBA-15].

Conflicts of Interest: The authors declare that they have no known competing financial interests or personal relationships that could have appeared to influence the work reported in this paper.

References

1. Yang, H.H.; Wang, L.G.; Xu, S.; Hui, X.; Cao, Y.; He, P.; Li, Y.; Li, H.Q. Highly dispersed Ru anchored on nanosheet N-doped carbon for efficient and chemoselective hydrogenation of nitroaromatics to aromatic amines under mild conditions. *Chem. Eng. J.* **2022**, *431*, 133863. [[CrossRef](#)]
2. Wu, S.T.; Huang, X.; Zhang, H.L.; Wei, Z.D.; Wang, M. Efficient Electrochemical Hydrogenation of Nitroaromatics into Arylamines on a CuCo_2O_4 Spinel Cathode in an Alkaline Electrolyte. *ACS Catal.* **2022**, *12*, 58–65. [[CrossRef](#)]
3. Zhang, L.K.; Shang, N.Z.; Gao, S.T.; Wang, J.M.; Meng, T.; Du, C.C.; Shen, T.D.; Huang, J.Y.; Wu, Q.H.; Wang, H.J.; et al. Atomically Dispersed Co Catalyst for Efficient Hydrodeoxygenation of Lignin-Derived Species and Hydrogenation of Nitroaromatics. *ACS Catal.* **2020**, *10*, 8672–8682. [[CrossRef](#)]
4. Sun, L.Q.; Zhu, L.; Qian, K.D.; Qin, B.J.; Huang, L.; Chen, C.H.; Lee, K.H.; Xie, L. Design, Synthesis, and Preclinical Evaluations of Novel 4-Substituted 1,5-Diarylanilines as Potent HIV-1 Non-Nucleoside Reverse Transcriptase Inhibitor (NNRTI) Drug Candidates. *J. Med. Chem.* **2012**, *55*, 7219–7229. [[CrossRef](#)]
5. Zhu, D.Q.; Liu, Q.; Luo, B.L.; Chen, M.H.; Pi, R.B.; Huang, P.; Wen, S.J. Synthesis of Carbazoles via One-Pot Copper-Catalyzed Amine Insertion into Cyclic Diphenyliodoniums as a Strategy to Generate a Drug-Like Chemical Library. *Adv. Synth. Catal.* **2013**, *355*, 2172–2178. [[CrossRef](#)]
6. Eli, L.D.; Kavuri, S.M.; Liu, Z.Y.; Su, J.; Xiao, Y.; Qiao, B.T.; Ding, Y.J. NiO_x -promoted Cu-based catalysts supported on AISBA-15 for chemoselective hydrogenation of nitroarenes. *J. Catal.* **2022**, *416*, 332–343. [[CrossRef](#)]
7. Sui, D.J.; Mao, F.; Fan, H.P.; Qi, Z.L.; Huang, J. General Reductive Amination of Aldehydes and Ketones with Amines and Nitroaromatics under H_2 by Recyclable Iridium Catalysts. *Chin. J. Chem.* **2017**, *35*, 1371–1377. [[CrossRef](#)]
8. Gutmann, B.; Cantillo, D.; Kappe, C.O. Continuous-Flow Technology—A Tool for the Safe Manufacturing of Active Pharmaceutical Ingredients. *Angew. Chem. Int. Ed.* **2015**, *54*, 6688–6728. [[CrossRef](#)]
9. Kreissl, H.; Jin, J.; Lin, S.H.; Schuette, D.; Stortte, S.; Levin, N.; Chaudret, B.; Vorholt, A.J.; Bordet, A.; Leitner, W. Commercial $\text{Cu}_2\text{Cr}_2\text{O}_5$ Decorated with Iron Carbide Nanoparticles as a Multifunctional Catalyst for Magnetically Induced Continuous-Flow Hydrogenation of Aromatic Ketones. *Angew. Chem. Int. Ed.* **2021**, *60*, 26639–26646. [[CrossRef](#)]
10. Wen, Z.H.; Yang, M.; Zhao, S.N.; Zhou, F.; Chen, G.W. Kinetics study of heterogeneous continuous-flow nitration of trifluoromethoxybenzene. *React. Chem. Eng.* **2018**, *3*, 379–387. [[CrossRef](#)]
11. Wang, F.J.; Chen, A.; Ling, S.D.; Xu, J.H. Continuous-flow diazotization of red base KD hydrochloride suspensions in a microreaction system. *React. Chem. Eng.* **2021**, *6*, 1462–1474. [[CrossRef](#)]
12. Lebl, R.; Zhu, Y.T.; Ng, D.; Hornung, C.H.; Cantillo, D.; Kappe, C.O. Scalable continuous flow hydrogenations using Pd/ Al_2O_3 -coated rectangular cross-section 3D-printed static mixers. *Catal. Today* **2022**, *383*, 55–63. [[CrossRef](#)]
13. Braun, M.; Esposito, D. Hydrogenation Properties of Nanostructured Tungsten Carbide Catalysts in a Continuous-Flow Reactor. *ChemCatChem* **2017**, *9*, 393–397. [[CrossRef](#)]
14. Davis, B.A.; Bennett, J.A.; Genzer, J.; Efimenko, K.; Abolhasani, M. Intensified Hydrogenation in Flow Using a Poly(beta-cyclodextrin) Network-Supported Catalyst. *ACS Sustain. Chem. Eng.* **2022**, *10*, 15987–15998. [[CrossRef](#)]
15. Zhang, Y.; Cheng, Y.J.; Wang, X.L.; Sun, Q.D.; He, X.H.; Ji, H.B. Enhanced Hydrogenation Properties of Pd Single Atom Catalysts with Atomically Dispersed Ba Sites as Electronic Promoters. *ACS Catal.* **2022**, *12*, 15091–15096. [[CrossRef](#)]
16. Huang, L.; Tang, F.Y.; Hao, F.; Zhao, H.; Liu, W.Y.; Lv, Y.; Liu, P.L.; Xiong, W.; Luo, H.A. Tuning the Electron Density of Metal Nickel via Interfacial Electron Transfer in Ni/MCM-41 for Efficient and Selective Catalytic Hydrogenation of Halogenated Nitroarenes. *ACS Sustain. Chem. Eng.* **2022**, *10*, 2947–2959. [[CrossRef](#)]
17. Couto, C.S.; Madeira, L.M.; Nunes, C.P.; Araujo, P. Commercial catalysts screening for liquid phase nitrobenzene hydrogenation. *Appl. Catal. A* **2016**, *522*, 152–164. [[CrossRef](#)]

18. Brandi, F.; Baumel, M.; Molinari, V.; Shekova, I.; Laueremann, I.; Heil, T.; Antonietti, M.; Al-Naji, M. Nickel on nitrogen-doped carbon pellets for continuous-flow hydrogenation of biomass-derived compounds in water. *Green Chem.* **2020**, *22*, 2755–2766. [[CrossRef](#)]
19. Cova, C.M.; Zuliani, A.; Manno, R.; Sebastian, V.; Luque, R. Scrap waste automotive converters as efficient catalysts for the continuous-flow hydrogenations of biomass derived chemicals. *Green Chem.* **2020**, *22*, 1414–1423. [[CrossRef](#)]
20. Geier, D.; Schnitz, P.; Walkowiak, J.; Leitner, W.; Francio, G. Continuous Flow Asymmetric Hydrogenation with Supported Ionic Liquid Phase Catalysts Using Modified CO₂ as the Mobile Phase: From Model Substrate to an Active Pharmaceutical Ingredient. *ACS Catal.* **2018**, *8*, 3297–3303. [[CrossRef](#)]
21. Wei, J.; Sun, Z.K.; Luo, W.; Li, Y.H.; Elzatahry, A.A.; Al-Enizi, A.M.; Deng, Y.H.; Zhao, D.Y. New Insight into the Synthesis of Large-Pore Ordered Mesoporous Materials. *J. Am. Chem. Soc.* **2017**, *139*, 1706–1713. [[CrossRef](#)] [[PubMed](#)]
22. Consolati, G.; Ferragut, R.; Galarneau, A.; Renzo, F.; Quasso, F. Mesoporous materials for antihydrogen production. *Chem. Soc. Rev.* **2013**, *42*, 3821–3832. [[CrossRef](#)] [[PubMed](#)]
23. Park, S.S.; Ha, C.S. Hollow Mesoporous Functional Hybrid Materials: Fascinating Platforms for Advanced Applications. *Adv. Funct. Mater.* **2018**, *28*, 1703814. [[CrossRef](#)]
24. Chen, C.; Li, B.X.; Zhou, L.J.; Xia, Z.F.; Feng, N.J.; Ding, J.; Wang, L.; Wan, H.; Guan, G.F. Synthesis of Hierarchically Structured Hybrid Materials by Controlled Self-Assembly of Metal Organic Framework with Mesoporous Silica for CO₂ Adsorption. *ACS Appl. Mater. Interfaces* **2017**, *9*, 23060–23071. [[CrossRef](#)]
25. Szczesniak, B.; Choma, J.; Jaroniec, M. Effect of graphene oxide on the adsorption properties of ordered mesoporous carbons toward H₂, C₆H₆, CH₄ and CO₂. *Microporous Mesoporous Mater.* **2018**, *261*, 105–110. [[CrossRef](#)]
26. Yao, J.F.; Dong, F.; Xu, X.; Wen, M.; Ji, Z.Y.; Feng, H.; Wang, X.L.; Tang, Z.C. Rational Design and Construction of Monolithic Ordered Mesoporous Co₃O₄@SiO₂ Catalyst by a Novel 3D Printed Technology for Catalytic Oxidation of Toluene. *ACS Appl. Mater. Interfaces* **2022**, *14*, 22170–22185. [[CrossRef](#)]
27. Bhat, A.; Hill, A.J.; Fisher, G.B.; Schwank, J.W. Improving the thermal stability and n-butanol oxidation activity of Ag-TiO₂ catalysts by controlling the catalyst architecture and reaction conditions. *Appl. Catal. B* **2021**, *297*, 120476. [[CrossRef](#)]
28. Liu, Q.; Zhong, Z.Y.; Gu, F.N.; Wang, X.Y.; Lu, X.P.; Li, H.F.; Xu, G.W.; Su, F.B. CO methanation on ordered mesoporous Ni-Cr-Al catalysts: Effects of the catalyst structure and Cr promoter on the catalytic properties. *J. Catal.* **2016**, *337*, 221–232. [[CrossRef](#)]
29. Xun, S.H.; Hou, C.Z.; Li, H.P.; He, M.Q.; Ma, R.L.; Zhang, M.; Zhu, W.S.; Li, H.M. Synthesis of WO₃/mesoporous ZrO₂ catalyst as a high-efficiency catalyst for catalytic oxidation of dibenzothiophene in diesel. *J. Mater. Sci.* **2018**, *53*, 15927–15938. [[CrossRef](#)]
30. Yang, P.D.; Zhao, D.Y.; Chmelka, B.F.; Stucky, G.D. Triblock-copolymer-directed syntheses of large-pore mesoporous silica fibers. *Chem. Mater.* **1998**, *10*, 2033–2036. [[CrossRef](#)]
31. Zhao, D.Y.; Huo, Q.S.; Feng, J.L.; Chmelka, B.F.; Stucky, G.D. Nonionic triblock and star diblock copolymer and oligomeric surfactant syntheses of highly ordered, hydrothermally stable, mesoporous silica structures. *J. Am. Chem. Soc.* **1998**, *120*, 6024–6036. [[CrossRef](#)]
32. Roucher, A.; Bentaleb, A.; Laurichesse, E.; Dourges, M.A.; Emo, M.; Schmitt, V.; Blin, J.L.; Backov, R. First Macro-Mesocellular Silica SBA-15-Si(HIPE) Monoliths: Conditions for Obtaining Self-Standing Materials. *Chem. Mater.* **2018**, *30*, 864–873. [[CrossRef](#)]
33. Yuan, P.; Tan, L.; Pan, D.H.; Guo, Y.N.; Zhou, L.; Yang, J.; Zou, J.; Yu, C.Z. A systematic study of long-range ordered 3D-SBA-15 materials by electron tomography. *New J. Chem.* **2011**, *35*, 2456–2461. [[CrossRef](#)]
34. Rettenmaier, C.; Aran-Ais, R.M.; Timoshenko, J.; Rizo, R.; Jeon, H.S.; Kuhl, S.; Chee, S.W.; Bergmann, A.; Roldan Cuenya, B. Enhanced Formic Acid Oxidation over SnO₂-decorated Pd Nanocubes. *ACS Catal.* **2020**, *10*, 14540–14551. [[CrossRef](#)] [[PubMed](#)]
35. Zeng, X.; Bai, Y.; Choi, S.M.; Tong, L.; Aleisa, R.M.; Li, Z.; Liu, X.; Yu, R.; Myung, N.V.; Yin, Y. Mesoporous TiO₂ nanospheres loaded with highly dispersed Pd nanoparticles for pH-universal hydrogen evolution reaction. *Mater. Today Nano* **2019**, *6*, 100038. [[CrossRef](#)]
36. Kirsch, P.D.; Ekerdt, J.G. Interfacial chemistry of the Sr/SiO_xN_y/Si(100) nanostructure. *J. Vac. Sci. Technol. A Vac. Surf. Film.* **2001**, *19*, 2222–2231. [[CrossRef](#)]
37. Celebioglu, A.; Topuz, F.; Uyar, T. Facile and green synthesis of palladium nanoparticles loaded into cyclodextrin nanofibers and their catalytic application in nitroarene hydrogenation. *New J. Chem.* **2019**, *43*, 3146–3152. [[CrossRef](#)]
38. Navaladian, S.; Viswanathan, B.; Varadarajan, T.K.; Viswanath, R.P. A Rapid Synthesis of Oriented Palladium Nanoparticles by UV Irradiation. *Nanoscale Res. Lett.* **2009**, *4*, 181–186. [[CrossRef](#)]
39. Liang, W.K.; Wang, Y.W.; Zhao, L.; Guo, W.; Li, D.; Qin, W.; Wu, H.H.; Sun, Y.H.; Jiang, L. 3D Anisotropic Au@Pt-Pd Hemispherical Nanostructures as Efficient Electrocatalysts for Methanol, Ethanol, and Formic Acid Oxidation Reaction. *Adv. Mater.* **2021**, *33*, 2100713. [[CrossRef](#)]
40. Kim, M.C.; Han, G.H.; Xiao, X.Y.; Song, J.; Hong, J.; Jung, E.; Kim, H.K.; Ahn, J.P.; Han, S.S.; Lee, K.Y.; et al. Anisotropic growth of Pt on Pd nanocube promotes direct synthesis of hydrogen peroxide. *Appl. Surf. Sci.* **2021**, *562*, 150031. [[CrossRef](#)]
41. Rajadhyaksha, R.A.; Karwa, S.L. Solvent effects in catalytic hydrogenation. *Chem. Eng. Sci.* **1986**, *41*, 1765–1770. [[CrossRef](#)]
42. Ding, S.M.; Cheng, D.; Xiao, W.M.; Ma, X.H.; Zeng, R.; Liu, S.Q.; Liang, S.Q.; Chen, C.; Song, W.G. Nickel Nanoparticles Encapsulated in Carbon Nanotubes as an Efficient and Robust Catalyst for Hydrogenation of Nitroarenes. *Catal. Lett.* **2023**, *153*, 595–604. [[CrossRef](#)]
43. Krishnan, S.; Patel, P.N.; Balasubramanian, K.K.; Chadha, A. Yeast supported gold nanoparticles: An efficient catalyst for the synthesis of commercially important aryl amines. *New J. Chem.* **2021**, *45*, 1915–1923. [[CrossRef](#)]

44. Kara, B.Y.; Kilbas, B.; Goksu, H. Selectivity and activity in catalytic hydrogenation of azido groups over Pd nanoparticles on aluminum oxy-hydroxide. *New J. Chem.* **2016**, *40*, 9550–9555. [[CrossRef](#)]
45. Zhang, R.K.; Chen, T.; Wang, G.S.; Guan, Y.Q.; Yan, G.Y.; Chen, Z.P.; Hu, J.S. Magnetic Recyclable Cu/ZnFe₂O₄ for Catalytic Reduction of Nitroarenes and C-N Bond Formation Reactions. *Catal. Lett.* **2022**, *152*, 3506–3516. [[CrossRef](#)]
46. Qu, Z.H.; Chen, X.; Zhong, S.; Deng, G.J.; Huang, H.W. NaI/PPh₃-Mediated Photochemical Reduction and Amination of Nitroarenes. *Org. Lett.* **2021**, *23*, 5349–5353. [[CrossRef](#)]
47. Almeida, A.F.; Ataide, F.A.P.; Loureiro, R.M.S.; Moreira, R.; Rodrigues, T. Augmenting Adaptive Machine Learning with Kinetic Modeling for Reaction Optimization. *J. Org. Chem.* **2021**, *86*, 14192–14198. [[CrossRef](#)]
48. Guo, B.B.; de Vries, J.G.; Otten, E. Hydration of nitriles using a metal-ligand cooperative ruthenium pincer catalyst. *Chem. Sci.* **2019**, *10*, 10647–10652. [[CrossRef](#)]
49. Quinn, J.F.; Bryant, C.E.; Golden, K.C.; Gregg, B.T. Rapid reduction of heteroaromatic nitro groups using catalytic transfer hydrogenation with microwave heating. *Tetrahedron Lett.* **2010**, *51*, 786–789. [[CrossRef](#)]
50. Chang, J.B.; Hwang, J.H.; Park, J.S.; Kim, J.P. The effect of dye structure on the dyeing and optical properties of dichroic dyes for PVA polarizing film. *Dye. Pigm.* **2011**, *88*, 366–371. [[CrossRef](#)]
51. Uberman, P.M.; Garcia, C.S.; Rodriguez, J.R.; Martin, S.E. PVP-Pd nanoparticles as efficient catalyst for nitroarene reduction under mild conditions in aqueous media. *Green Chem.* **2017**, *19*, 739–748. [[CrossRef](#)]
52. Duan, X.N.; Wang, X.P.; Chen, X.K.; Zhang, J.S. Continuous and Selective Hydrogenation of Heterocyclic Nitroaromatics in a Micropacked Bed Reactor. *Org. Process Res. Dev.* **2021**, *25*, 2100–2109. [[CrossRef](#)]
53. Yue, S.N.; Wang, X.G.; Li, S.T.; Sheng, Y.; Zou, X.J.; Lu, X.G.; Zhang, C.L. Highly selective hydrogenation of halogenated nitroarenes over Ru/CN nanocomposites by *in situ* pyrolysis. *New J. Chem.* **2020**, *44*, 11861–11869. [[CrossRef](#)]
54. Guo, Y.Y.; Li, Z.H.; Xia, T.Y.; Du, Y.L.; Mao, X.M.; Li, Y.Q. Molecular mechanism of azoxy bond formation for azoxymycins biosynthesis. *Nat. Commun.* **2019**, *10*, 4420. [[CrossRef](#)]
55. Dong, Z.Y.; Wen, Z.H.; Zhao, F.; Kuhn, S.; Noël, T. Scale-up of micro- and milli-reactors: An overview of strategies, design principles and applications. *Chem. Eng. Sci. X* **2021**, *10*, 100097. [[CrossRef](#)]
56. Mohammad, N.; Chukwudoro, C.; Bepari, S.; Basha, O.; Aravamudhan, S.; Kuila, D. Scale-up of high-pressure F-T synthesis in 3D printed stainless steel microchannel microreactors: Experiments and modeling. *Catal. Today* **2022**, *397*, 182–196. [[CrossRef](#)]
57. Zhu, Z.G.; Yang, L.; Yu, Y.X.; Zhang, L.J.; Tao, S.Y. Scale-up Design of a Fluorescent Fluid Photochemical Microreactor by 3D Printing. *ACS Omega* **2020**, *5*, 7666–7674. [[CrossRef](#)]

Disclaimer/Publisher's Note: The statements, opinions and data contained in all publications are solely those of the individual author(s) and contributor(s) and not of MDPI and/or the editor(s). MDPI and/or the editor(s) disclaim responsibility for any injury to people or property resulting from any ideas, methods, instructions or products referred to in the content.